Open Access

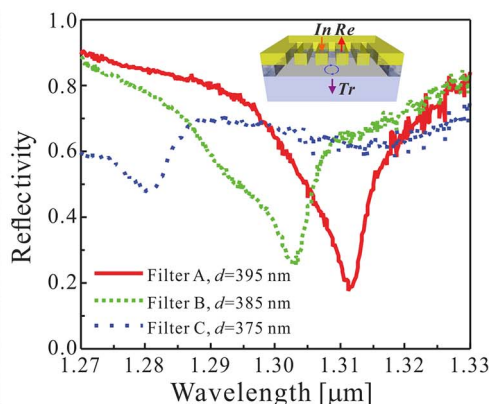# Fabrication and Characterization of Integrable GaAs-Based High-Contrast Grating Reflector and Fabry–Pérot Filter Array With GaInP Sacrificial Layer

Anjin Liu
Philip Wolf
Jan-Hindrik Schulze
Dieter Bimberg, Fellow, IEEE

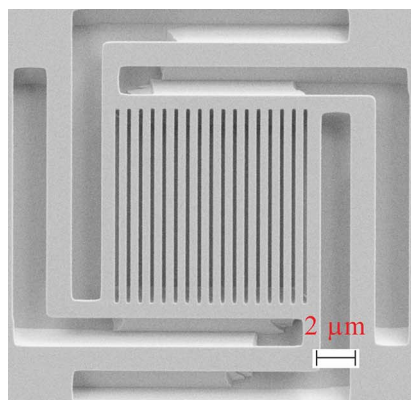# Fabrication and Characterization of Integrable GaAs-Based High-Contrast Grating Reflector and Fabry–Pérot Filter Array With GaInP Sacrificial Layer

Anjin Liu,[1,2] **Philip Wolf,**[1] **Jan-Hindrik Schulze,**[1] **and Dieter Bimberg,**[1,3] *Fellow, IEEE*

[1]Institut für Festkörperphysik und Zentrum für Nanophotonik, Technische Universität Berlin, 10623 Berlin, Germany
[2]Laboratory of Solid-State Optoelectronics Information Technology, Institute of Semiconductors, CAS, Beijing, China
[3]King Abdulaziz University, Jeddah, KSA

Abstract: Integrable GaAs-based high-contrast gratings (HCGs) are fabricated and characterized, targeting applications in high-speed vertical-cavity surface-emitting lasers (VCSELs). A $Ga_{0.51}In_{0.49}P$ sacrificial layer beneath the GaAs layer is employed to create a low index surrounding HCG strips by selective etching. Experimental results show that the finite-size HCG has a reflectivity of 93% from 1270 to 1330 nm for the transverse magnetic polarization, which is consistent with the calculated results. An HCG-based Fabry–Pérot filter array formed by the different HCGs, air gap, and GaAs substrate is demonstrated. The measured resonance wavelengths of the filter arrays are consistent with the theoretical results, which implies that the resonance wavelength of such filters can be tuned by parameters of the HCG itself.

Index Terms: Gratings, subwavelength structures, mirrors, vertical-cavity surface-emitting laser (VCSEL), wavelength filtering devices.

1. Introduction

High-speed vertical-cavity surface-emitting lasers (VCSELs) have attracted intense attention for long time, because VCSELs are low-cost and energy-efficient sources for optical interconnects in data centers, high-performance computer systems, and other short-reach networks [1]–[6]. Very recently, directly modulated 850-nm VCSELs with 71 Gbit/s data rates at room temperature have been reported [7]. Record energy efficiency of 56 fJ/bit dissipated energy and 46 Gbit/s with data rate at 85 degrees were demonstrated [8], [9]. These exciting results are achieved by the adoption of a short cavity, optimization of the photon lifetime, advanced active region design, good thermal management. Even though higher order modulation formats, advanced driver chips, and superior photoreceiver systems are beneficial to achieve still lager data rates [7], [10], improving the performance of the VCSEL itself is essential. To further increase the capacity of a link, wavelength-division multiplexing (WDM) with high-speed VCSEL arrays on the same wafer using

multiple uniformly spaced wavelengths transmitted in a single fiber are used, which makes the link very low-cost, compact, and energy-efficient.

One promising approach to improve the bandwidth of a single VCSEL is adopting novel surface nanostructures. Recently, high-contrast gratings (HCGs) with grating strips fully surrounded by a low-index medium like air, demonstrated high reflectivity over a broad band [11]–[15]. The high reflectivity over a broad band is originating from the destructive interference at the output plane of the HCG, and the large index contrast between the HCG strips and the low-index medium [11]. HCGs have been intensively explored and have been employed in, for example, lasers [11], [12], flat optics [11], [16], and optical sensors [11], [17]. One typical application of HCGs is for broadband and high-reflectivity reflectors to replace at least part of the top Distributed Bragg reflector (DBR) of VCSELs. The first electrically pumped HCG-VCSEL was demonstrated by employing AlGaAs-based HCG at 850 nm [11]. Later, 1060-nm and 1550-nm HCG-VCSELs were developed [18], [19]. HCG-VCSELs exhibit single-mode output with polarized light, because high-order modes have higher loss introduced by the HCG and the HCG shows polarization selectivity. Furthermore, HCGs have a smaller energy penetration depth compared with DBR, which contributes to a larger confinement factor of HCG-VCSELs [20]. This larger confinement factor increases the relaxation resonance frequency of a laser [21]. Therefore, HCG-VCSELs are expected to achieve a higher modulation speed. In [22], it is predicted that HCG-VCSELs can reach an ultrahigh data rate beyond 100 Gbit/s.

As mentioned above, WDM is a promising way to increase the bandwidth of a single fiber. Low-cost, energy-efficient, high-speed, and monolithically integrated multi-wavelength VCSEL arrays are highly desirable. For conventional VCSEL structures composed of top DBR, cavity, and bottom DBR, the resonance wavelength of the VCSEL is determined by the round-trip phase condition of the effective cavity and is fixed after VCSEL wafer growth. Several methods for multi-wavelength VCSEL arrays on a single wafer by locally varying the layer thickness in the cavity, such as growth on nonplanar substrate by metalorganic chemical vapor deposition [23] and patterned-substrate molecular beam epitaxy growth [24], were proposed and demonstrated. However, such methods are very complex. Recently, HCG-VCSEL arrays were proposed for WDM applications to increase the aggregate bandwidth of a single fiber [25]. The reflection phase of the HCG with a fixed thickness can be tuned by the period and duty cycle (defined as the ratio of HCG strip width to HCG period). Thus, it is very easy to design and fabricate monolithic multi-wavelength VCSEL arrays on the same HCG-VCSEL wafer, which can be realized in the standard wafer growth.

Up to now, many kinds of HCGs based on different material systems have been successfully developed. Suspended HCGs employing AlGaAs(GaAs) for 850 nm [11], GaAs(AlInP) for 1060 nm [18], and InP(InGaAs) for 1550 nm [26], have been used for HCG-based photonic devices (the materials in the brackets are used for sacrificial layers for creating the air gap). The suspended HCGs are very flexible and good candidates for tunable VCSELs [18], [27] and tunable filters [26]. For good mechanical stability, Silicon/SiO_2 [28] and GaAs/Al_2O_3 [29] material systems with a high index contrast have been used in HCG-VCSELs. In this work, we design, fabricate, and characterize integrable GaAs-based HCGs with $Ga_{0.51}In_{0.49}P$ as the sacrificial layer, targeting applications for high-speed VCSELs and its array in the wavelength range of 1300 nm. In contrast to GaAs(AlInP) and GaAs(AlGaAs) material systems for GaAs-based HCGs which contain Al in the sacrificial layers, we use $Ga_{0.51}In_{0.49}P$, which is lattice matched to GaAs and also has a high etching selectivity to GaAs in the HCl etching solution, to serve as the sacrificial layer to avoid the problem of oxidation of the remaining sacrificial layer [30]. Additionally, a 1×3 HCG-based Fabry-Pérot filter array composed of HCGs, air gap, and GaAs substrate is demonstrated.

2. Structure and Design

The HCG structures studied here are schematically shown in Fig. 1(a) and a scanning electron microscope (SEM) image of a HCG is shown in Fig. 1(b). The reflectivity of the HCG depends on the polarization. In the transverse magnetic (TM) polarization, the electric component is
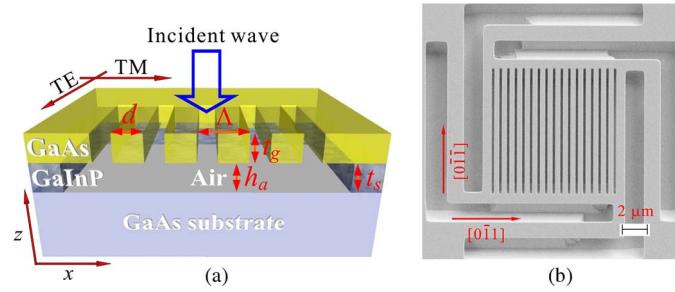
Fig. 1. (a) Schematic of the HCG. Λ is the period of the HCG; d is the width of the strips; t_g is the thickness of the GaAs layer; h_a is the thickness of the air gap after selective etching and grating release; t_s the thickness of the $Ga_{0.51}In_{0.49}P$ sacrificial layer. TE means transverse electric, where the electric component is parallel to the HCG strips. TM means transverse magnetic, where the electric component is perpendicular to the strips. The arrow denotes the incident wave. (b) Scanning electron microscope image of the fabricated HCG after selective etching and grating release. The arrows represent the crystal orientations. The size of the HCG is 10 μm $\times$ 10 μm.
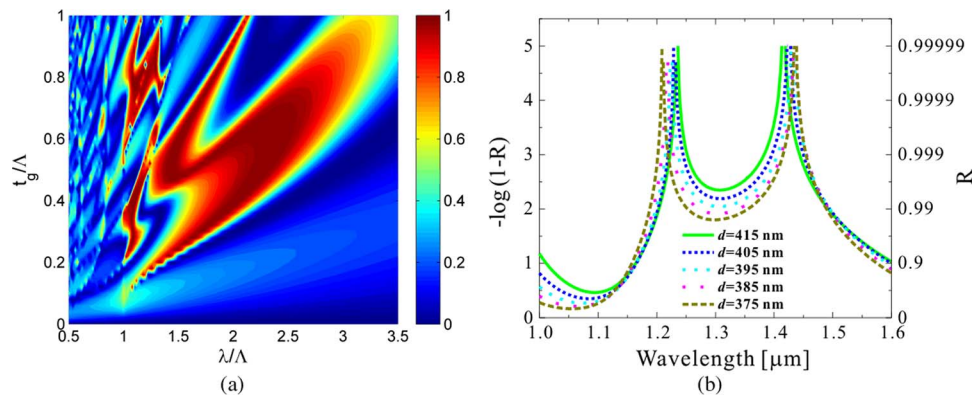

Fig. 2. (a) Reflectivity contour of the HCG as a function of normalized thickness (t_g/Λ) and normalized wavelength (λ/Λ) under normal incidence at DC = 0.65 (duty cycle, DC, is defined as d/Λ). (b) Reflectivity spectra for different widths of the HCG strip under the TM polarization using RCWA method; $\Lambda = 600$ nm, and $t_g = 362$ nm.

perpendicular to the HCG strips, whereas the electric component is parallel to the HCG strips for the transverse electric (TE) polarization.

The parameters of the HCG reflector can be optimized by rigorous coupled wave analysis (RCWA) [31] and analytical methods [11]. The GaAs-based HCGs designed here are expected to have high reflectivity around 1300 nm, a wavelength range interesting for optical interconnects on computer chips. We focus on the TM polarization, because the evanescent tail through the output plane of the HCG is shorter than the TE polarization [13]. The shorter evanescent tail brings a smaller phase penetration depth, which can enhance the modulation speed [21]. The refractive index of GaAs used in the calculation is 3.4, and GaAs is assumed to be lossless and dispersion free for the present wavelength range. Fig. 2(a) is a reflectivity contour of the HCG as a function of normalized thickness (t_g/Λ) and normalized wavelength (λ/Λ) under normal incidence for the incident wave using RCWA method. Thus, from Fig. 2(a), we can determine that for a wavelength around 1300 nm the period of the HCG is 600 nm, the thickness of the HCG layer is 362 nm. Fig. 2(b) shows that the reflectivity spectra of HCGs under varying width of the strips show high reflectivity across a large band.

3. Fabrication

The HCGs are fabricated on a wafer that is composed of a 362-nm GaAs layer, a 1-μm $Ga_{0.51}In_{0.49}P$ sacrificial layer, and a GaAs substrate. The HCG pattern is defined on the
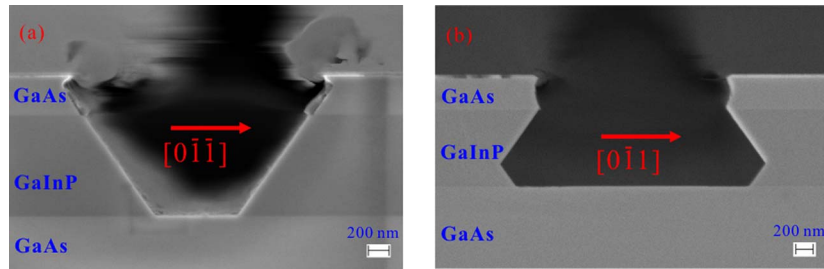
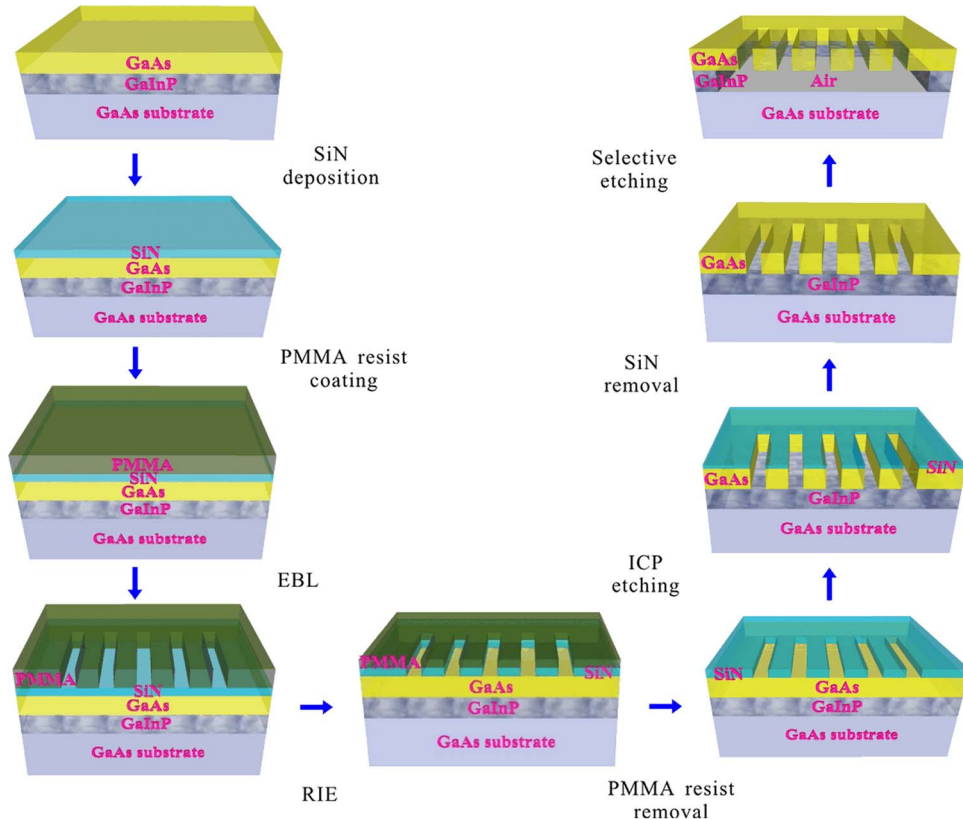Fig. 3. SEM images of the etching profile along $[0\bar{1}\bar{1}]$ (a) and $[0\bar{1}1]$ (b) directions.

Fig. 4. Schematic of the HCG fabrication process. PMMA: poly methyl methacrylate; EBL: electron beam lithography; RIE: reactive ion etching; ICP: inductively coupled plasma.

GaAs layer, and the $Ga_{0.51}In_{0.49}P$ sacrificial layer is selectively etched to create an air gap, as shown in Fig. 1(a). Etching of the $Ga_{0.51}In_{0.49}P$ sacrificial layer is carried out with the HCl solution [32]. Fig. 3 shows the SEM images of the etching profile along the $[0\bar{1}\bar{1}]$ and $[0\bar{1}1]$ directions. The etching rate depends on the crystal orientation and the concentration of HCl. Therefore, the HCG strips are arranged in the $[0\bar{1}1]$ direction to facilitate the selective etching when the HCG pattern is defined, as shown in Fig. 1(b).

The fabrication flow of the HCG is schematically shown in Fig. 4. The wafer is first deposited with Si_3N_4 by plasma-enhanced chemical vapor deposition (PECVD). PMMA electron resist is spinned and then electron beam lithography (EBL) is used for defining the grating pattern. After development, the grating pattern is transferred onto the Si_3N_4 layer by reactive ion etching (RIE) with a gas mixture of CHF_3/O_2. The grating structure is then transferred onto the GaAs layer with Si_3N_4 as the mask by inductively coupled plasma (ICP) etching with a gas mixture of
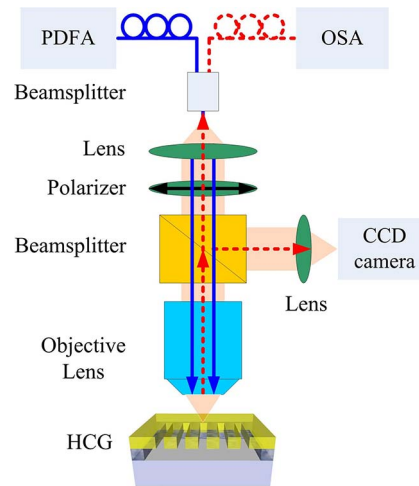
Fig. 5. Schematic of the optical measurement setup. PDFA: praseodymium-doped fiber amplifier; OSA: optical spectrum analyzer; CCD: charge-coupled device; HCG: high contrast grating. The blue solid line denotes the incident light, and the red dotted line denotes the reflected light.

$Cl_2/BCl_3/Ar$. To remove the $Ga_{0.51}In_{0.49}P$ sacrificial layer under the grating, the grating is placed in the HCl solution at room temperature. After selective etching, the grating is rinsed by deionized water and dried for grating release. The HCGs in the array have the same period and thickness, but the width of the HCG strips is varied with a step size of 10 nm. The SEM image of a 10 μm × 10 μm HCG after drying is shown in Fig. 1(b). As shown in Fig. 1(b), we deliberately leave some $Ga_{0.51}In_{0.49}P$ connecting the HCG to the substrate at the top edge and bottom edge of the HCG, because the remaining $Ga_{0.51}In_{0.49}P$ can serve as posts to support the HCG for easy grating release without critical point drying.

4. Characterization

The reflectivity spectra are measured with the setup schematically shown in Fig. 5. The broadband amplified spontaneous emission (ASE) (1270–1330 nm) from a praseodymium-doped fiber amplifier (PDFA) is collected by a fiber and then collimated by a lens. The light is polarized by a Glan-Thomson polarizer. Finally, the light is focused on the HCG by an objective lens with 50× magnification and numerical aperture (NA) of 0.45. The reflected light is collected by another fiber via a planar beam splitter and then measured by an optical spectrum analyzer (OSA). The reflected light is partly led by a cube beam splitter into a charge-coupled device (CCD) camera to observe the position of the HCG and estimate the spot size of the incident light on the HCG after the objective lens. The diameter of the focused spot size is about 4 μm. The reflectivity of a gold-coated mirror is measured for a reference. The reflectivity of the HCG is normalized to the reflectivity of the gold-coated mirror. For comparison, the reflectivity of the GaAs surface without the HCG pattern is also measured, which can clearly show the enhanced reflectivity after the GaAs surface is patterned with the HCG.

Fig. 6(a) shows the measured reflectivity spectrum of the HCG with a strip width of 410 nm measured by SEM. The measurement result verifies that the HCG has a reflectivity of over 93% from 1270 to 1330 nm. Because the HCG has a size of 10 μm × 10 μm and the spot size of the incident wave is about 4 μm in diameter, the reflectivity spectrum of this finite-size HCG is calculated by 3-dimensional finite-difference time-domain (3D-FDTD) method with perfectly matched layer boundary conditions [33] taking into account of the sidewall shape (negatively sloped) of the HCG strips after ICP etching. The simulation model includes the air gap and the substrate. Fig. 6(a) also shows that the measured reflectivity of the TM polarization is consistent with the simulation result. Note that TM-polarized reflectivity of polarization calculated by 3D-FDTD in Fig. 6(a) is lower than the calculated reflectivity by RCWA method because of the
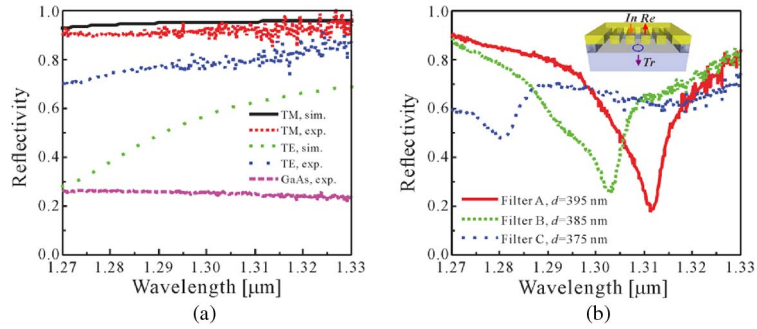
Fig. 6. (a) Calculated and measured reflectivity spectra of the HCG with a strip width of 410 nm. (b) Reflectivity spectra of the 1 × 3 HCG-based Fabry-Pérot filter array. The inset is the schematic of the filter. *In*, *Re*, and *Tr* in the insets represent the incident wave, reflected wave, and transmitted wave, respectively.
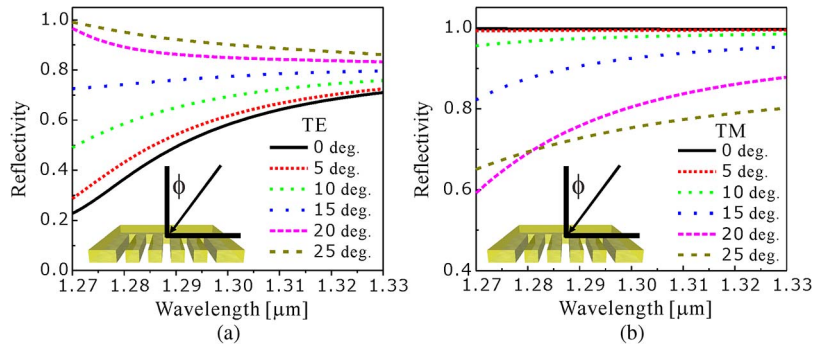

Fig. 7. (a) Calculated reflectivity spectra of the HCG (including air gap and substrate) with a strip width of 410 nm for TE (a) and TM (b) polarizations under different angles of incidence (ϕ). The simulation model takes into account of the sidewall shape (negatively sloped) of HCG strips after ICP etching.

different boundary conditions used in the calculations [33]. For the TE polarization, there is a difference between the simulation result and the experimental result. This difference is caused by the higher-order components in the focused incident wave after the objective lens with a high NA. As shown in Fig. 7 the reflectivity increases as the angle of incidence increases for the TE polarization, whereas the reflectivity decreases as the angle of incidence increases for the TM polarization. For comparison, the reflectivity of the GaAs surface without a HCG pattern is also measured to be 26%, as shown in Fig. 6(a), which is close to the theoretical value of 29.8%.

In these HCGs, the $Ga_{0.51}In_{0.49}P$ sacrificial layer is removed by HCl, and the smooth GaAs surface beneath the HCG is exposed. The GaAs surface can serve as a mirror with a reflectivity of 29.8%. Thus, the HCG, air gap, and GaAs surface can compose a Fabry-Pérot filter. The resonance wavelength of the filter is determined by the equation $\varphi_{GaAs} + \varphi_{HCG} + 4 \times h_a \times \pi/\lambda = 2 \times \pi \times m$ ($m = 0, 1, 2, 3, \ldots$) known as the phase matching condition, where φ_{GaAs} is the reflection phase of the GaAs/air interface, φ_{HCG} is the reflection phase of the HCG, λ is the wavelength in the free space, and h_a is the thickness of the air gap. When the incident wavelength satisfies the phase matching condition, the resonance in the filter happens and a low reflectivity at the resonance wavelength occurs in the reflectivity spectrum. Theoretically the HCG shown in Fig. 6(a) also can form a Fabry-Pérot filter with the GaAs substrate and the air gap. Because of the limited bandwidth of the available optical source, the resonance wavelength is not observed in the reflectivity spectrum of the HCG with the strip width of 410 nm. Therefore, within the wavelength range of from 1270 to 1330 nm, the substrate beneath the HCG has little effect on the reflectivity spectrum.
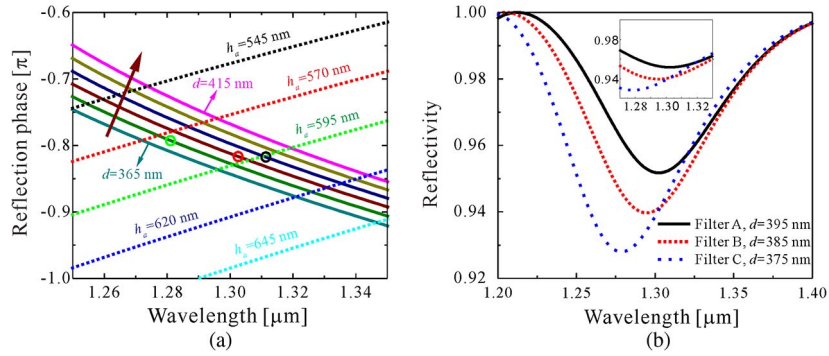
Fig. 8. (a) Contour plot of resonance wavelengths of the filters composed of different HCGs and different air gap thicknesses ($\Lambda = 600$ nm and $t_g = 362$ nm). The solid lines represent the reflection phases of the HCGs with different widths (d) of the strip with a step size of 10 nm from 365 to 415 nm. The dotted lines represent variations of the air gap (h_a), with a step size of 25 nm from 545 to 645 nm. The intersections of the lines represent the resonance wavelengths of filters with the corresponding air gap and the corresponding width of the HCG strip. The black, red, and blue circles denote the resonance wavelengths of Filters A, B, and C, respectively. The arrows indicate the direction of increase. (b) Calculated spectra of the filters.

However, the resonance wavelength of the Fabry-Pérot filter can be observed when the resonance wavelength is within the wavelength range of from 1270 to 1330 nm. Fig. 6(b) shows the reflectivity spectra of three Fabry-Pérot filters in the 1×3 array composed of three adjacent HCGs with different widths of the HCG strips. The widths of the HCG strips in the three filters measured by SEM are 395 nm (Filter A), 385 nm (Filter B), and 375 nm (Filter C), respectively. The resonance wavelengths of Filters A, B, and C are 1311.5, 1302.6, and 1280.9 nm, respectively. The calculated reflection phase spectra of the three HCGs by RCWA method are shown in Fig. 8(a). At the resonance wavelengths, the reflection phase of the HCG in Filter A is $-0.818 \times \pi$, $-0.816 \times \pi$ for the HCG in Filter B, and $-0.793 \times \pi$ for the HCG in Filter C. Therefore, the thickness of the air gap can be obtained by the above-mentioned phase matching condition. The thickness of the air gap in Filter A is 596 nm, 591 nm in Filter B, and 574 nm in Filter C. Note that the air gaps in the filters are formed by removing the $Ga_{0.51}In_{0.49}P$ sacrificial layer. Nominally, the thickness of the air gap in the filters is equal to the thickness of the $Ga_{0.51}In_{0.49}P$ sacrificial layer. In fact the suspended HCG is displaced down to the substrate after the sacrificial layer is removed [26]. Thus, the thickness h_a of the air gap is not equal to the thickness t_s of the $Ga_{0.51}In_{0.49}P$ sacrificial layer. We find the thicknesses of the air gaps in the three filters are different. The HCGs in the three filters are with the same parameters, except for the width of the HCG strip. The reason is that the etching rate of the $Ga_{0.51}In_{0.49}P$ sacrificial layer in the $[0\overline{1}\overline{1}]$ direction depends on the air gaps between the HCG strips. The air gap between HCG strips is larger (the duty cycle, $DC = d/\Lambda$, is smaller), and the etching rate of the $Ga_{0.51}In_{0.49}P$ sacrificial layer is larger. Thus, as shown in Fig. 1(b) and Fig. 3(a), the heights of the upper and lower bases under the upper and lower edges of the HCG are smaller, resulting in a thickness of the air gap in the filter to be smaller.

We calculate the resonance wavelength of each filter in the filter array, as shown in Fig. 8(b). The calculated resonance wavelengths of Filters A, B, and C are 1302.9 nm, 1294.6 nm, and 1278.8 nm, respectively, consistent with the measured results (1311.5, 1302.6, and 1280.9 nm for Filters A, B, and C, respectively). Because of the low reflectivity of the GaAs surface after selective etching, the calculated Q factors (defined as $\lambda/\Delta\lambda$; λ, wavelength; $\Delta\lambda$, full width at half maximum of the resonance) of the three filters are 15. As shown in Fig. 6(b), the measured Q factors after fitting for the three filters are about 90. The measured Q factors are larger than the calculated ones probably caused by higher-order angular components in the focused incident wave after the high-NA objective lens. The measured reflectivity of Filter C in Fig. 6(b) is lower than the calculated one in Fig. 8(b), probably due to the large sensitivity of the reflectivity of Filter C to higher order angular components.

We calculate the reflection phases of the HCGs for different widths of the HCG strips, and resonance wavelengths of the Fabry-Pérot filter array composed of different thicknesses of air gaps and HCGs. As shown in Fig. 8(a), the reflection phase (the solid lines) increases as the width of the HCG strip increases. The dotted lines represent the thicknesses of the air gaps of the filters. The intersection of the solid line and the dotted line represents the resonance wavelength of the filter with the corresponding thickness of the air gap and the corresponding width of the HCG strip. The black, red, and blue circles in Fig. 8(a) denote the resonance wavelengths of Filters A, B, and C, respectively. With a fixed thickness of the air gap, the resonance wavelengths of the filter can be nearly linearly tuned by the width of the HCG strip with a fixed HCG period. This implies that high-speed HCG-VCSEL arrays for WDM applications can be fabricated by defining HCGs with different duty cycles with a fixed HCG period on the same HCG-VCSEL wafer. It should be noted that the resonance wavelengths of the filter can be nearly linearly tuned by the HCG period with a fixed width of the HCG strip for a fixed thickness of the air gap. Also for a specific HCG-VCSEL, the resonance wavelength of the filter can be nearly linearly tuned by changing the thickness of the air gap, which has been successfully employed in tunable HCG-VCSELs [27]. The resonance wavelengths of the 1×3 filter array in this work are not uniformly spaced because of the different thicknesses of the air gaps. Uniformly spaced resonance wavelengths of the filter array can be achieved by reducing the size of the two nearest air trenches out of the HCG part in the vertical directions to have identical thicknesses of the air gaps in each element of the filter array. Therefore, high-speed HCG-VCSEL arrays with uniformly spaced wavelengths on the same wafer are feasible.

5. Conclusion

In summary, we have designed, fabricated, and characterized integrable GaAs-based HCG reflectors for high-speed VCSELs and demonstrated a 1×3 HCG-based Fabry-Pérot filter array. A $Ga_{0.51}In_{0.49}P$ layer is used as the sacrificial layer to be removed to create the low-index surrounding (i.e., air) around the HCG strips. Our experiments show that HCGs can achieve a reflectivity of 93% from 1270 to 1330 nm, consistent with the simulation result. The measured reflectivity shows that the finite-size HCG has a high reflectivity and can serve as the mirror of a VCSEL or can replace most of layers of a DBR. By optimizing the oxide aperture and the size of the HCG, the threshold current can be in the sub-milliampere range with single-mode output, which is very helpful to realize energy-efficient and long-reach optical links. Because the smooth GaAs surface of the GaAs substrate after the removal of the $Ga_{0.51}In_{0.49}P$ sacrificial layer has a reflectivity of 30%, a 1×3 HCG-based Fabry-Pérot filter array is constructed with different HCGs, air gaps, and the smooth GaAs surface. The HCG-based Fabry-Pérot filter array exhibits three different resonance wavelengths on the same wafer, in agreement with the calculations. The results indicate that besides the reflectivity, the reflection phase of the HCG can be tailored by the parameters of the HCG. This work shows the promise of employing HCG reflectors to construct large-scale filter arrays and VCSEL arrays with uniformly spaced resonance wavelengths. This work is helpful to design and fabricate high-speed and energy-efficient GaAs-based HCG-VCSEL and its arrays for the WDM applications at 980 nm and beyond.

References

[1] D. Bimberg, "Ultrafast VCSELs for Datacom," *IEEE Photon. J.*, vol. 2, no. 2, pp. 273–275, Apr. 2010.

[2] F. Koyama, "Recent advances of VCSEL photonics," *J. Lightw. Technol.*, vol. 24, no. 12, pp. 4502–4513, Dec. 2006.

[3] A. Larsson, "Advances in VCSELs for communication and sensing," *IEEE J. Sel. Topics Quantum Electron.*, vol. 17, no. 6, pp. 1552–1567, Nov./Dec. 2011.

[4] R. Michalzik, *Vcsels-Fundamentals, Technology and Applications of Vertical-Cavity Surface-Emitting Lasers*, ser. Springer Series in Optical Sciences. New York, NY, USA: Springer-Verlag, vol. 166, 2013.

[5] A. F. Benner, M. Ignatowski, J. A. Kash, D. M. Kuchta, and M. B. Ritter, "Exploitation of optical interconnects in future server architectures," *IBM J. Res. Develop.*, vol. 49, no. 4/5, pp. 755–775, Jul. 2005.

[6] J. A. Tatum *et al.,* "VCSEL-based interconnects for current and future data centers," *J. Lightw. Technol.*, vol. 33, no. 4, pp. 727–732, Feb. 2015.

[7] D. M. Kuchta *et al.,* "A 71-Gb/s NRZ modulated 850-nm VCSEL-based optical link," *IEEE Photon. Technol. Lett.*, vol. 27, no. 6, pp. 577–580, Mar. 2015.

[8] P. Moser *et al.,* "56 fJ dissipated energy per bit of oxide-confined 850 nm VCSELs operating at 25 Gbit/s," *Electron. Lett.*, vol. 48, no. 20, pp. 1292–1294, Sep. 2012.

[9] P. Moser *et al.,* "Error-free 46 Gbit/s operation of oxide-confined 980 nm VCSELs at 85 °C," *Electron. Lett.*, vol. 50, no. 19, pp. 1369–1371, Sep. 2014.

[10] K. Szczerba, P. Westbergh, M. Karlsson, P. A. Andrekson, and A. Larsson, "70 Gbps 4-PAM and 56 Gbps 8-PAM using an 850 nm VCSEL," *J. Lightw. Technol.*, vol. 33, no. 7, pp. 1395–1401, Apr. 2015.

[11] C. J. Chang-Hasnain and W. Yang, "High-contrast gratings for integrated optoelectronics," *Adv. Opt. Photon.*, vol. 4, no. 3, pp. 379–440, 2012.

[12] S. Boutami, B. Benbakir, J.-L. Leclercq, and P. Viktorovitch, "Compact and polarization controlled 1.55 μm vertical-cavity surface emitting laser using single-layer photonic crystal mirror," *Appl. Phys. Lett.*, vol. 91, no. 7, Aug. 2007, Art. ID 071105.

[13] R. Magnusson and M. Shokooh-Saremi, "Physical basis for wideband resonant reflectors," *Opt. Exp.*, vol. 16, no. 5, pp. 3456–3462, Mar. 2008.

[14] P. Debernardi, R. Orta, T. Gründl, and M.-C. Amann, "3-D vectorial optical model for high-contrast grating vertical-cavity surface-emitting lasers," *IEEE J. Quantum Electron.*, vol. 49, no. 2, pp. 137–145, Feb. 2013.

[15] A. Liu, F. Fu, Y. Wang, B. Jiang, and W. Zheng, "Polarization-insensitive subwavelength grating reflector based on a semiconductor-insulator-metal structure," *Opt. Exp.*, vol. 20, no. 14, pp. 14 991–15 000, Jun. 2012.

[16] D. Fattal, J. Li, Z. Peng, M. Fiorentino, and R. G. Beausoleil, "Flat dielectric grating reflectors with focusing abilities," *Nature Photon.*, vol. 4, pp. 466–470, Jul. 2010.

[17] A. Liu, W. Hofmann, and D. Bimberg, "Integrated high-contrast-grating optical sensor using guided mode," *IEEE J. Quantum Electron.*, vol. 51, no. 1, Jan. 2015, Art. ID 6600108.

[18] T. Ansbæk, I.-S. Chung, E. S. Semenova, and K. Yvind, "1060-nm tunable monolithic high index contrast subwavelength grating VCSEL," *IEEE Photon. Technol. Lett.*, vol. 25, no. 4, pp. 365–367, Feb. 2013.

[19] J. Ferrara, W. Yang, L. Zhu, P. Qiao, and C. J. Chang-Hasnain, "Heterogeneously integrated long-wavelength VCSEL using silicon high contrast grating on an SOI substrate," *Opt. Exp.*, vol. 23, no. 3, pp. 2512–2523, Feb. 2015.

[20] D. Zhao, Z. Ma, and W. Zhou, "Field penetrations in photonic crystal Fano reflectors," *Opt. Exp.*, vol. 18, no. 13, pp. 14152–14158, Jun. 2010.

[21] L. Coldren and S. Corzine, *Diode Lasers and Photonic Integrated Circuits.* New York, NY, USA: Wiley, 1995.

[22] G. C. Park *et al.,* "Hybrid vertical-cavity laser with lateral emission into a silicon waveguide," *Laser Photon. Rev.*, vol. 9, no. 3, pp. L11–L15, May 2015.

[23] M. Arai *et al.,* "Multiple-wavelength GaInAs-GaAs vertical cavity surface emitting laser array with extended wavelength span," *IEEE J. Sel. Topics Quantum Electron.*, vol. 9, no. 5, pp. 1367–1373, Sep./Oct. 2003.

[24] W. Yuen, G. S. Li, and C. J. Chang-Hasnain, "Multiple-wavelength vertical-cavity surface-emitting laser arrays," *IEEE J. Sel. Topics Quantum Electron.*, vol. 3, no. 2, pp. 422–428, Apr. 1997.

[25] V. Karagodsky *et al.,* "Monolithically integrated multi-wavelength VCSEL arrays using high-contrast gratings," *Opt. Exp.*, vol. 18, no. 2, pp. 694–699, Jan. 2010.

[26] S. Boutami *et al.,* "Highly selective and compact tunable MOEMS photonic crystal Fabry–Pérot filter," *Opt. Exp.*, vol. 14, no. 8, pp. 3129–3137, Apr. 2006.

[27] M. C. Y. Huang, Y. Zhou, and C. J. Chang-Hasnain, "A nanoelectromechanical tunable laser," *Nature Photon.*, vol. 2, pp. 180–184, Feb. 2008.

[28] W. Hofmann *et al.,* "Long-wavelength high-contrast grating vertical-cavity surface-emitting laser," *IEEE Photon. J.*, vol. 2, no. 3, pp. 415–422, Jun. 2010.

[29] Y. Laaroussi *et al.,* "Oxide confinement and high contrast grating mirrors for Mid-infrared VCSELs," *Opt. Mater. Exp.*, vol. 3, no. 10, pp. 1576–1585, Oct. 2013.

[30] E. Weidner *et al.,* "Achievement of ultrahigh quality factors in GaAs photonic crystal membrane nanocavity," *Appl. Phys. Lett.*, vol. 89, no. 22, 2006, Art. ID 221104.

[31] M. G. Moharam and T. K. Gaylord, "Rigorous coupled-wave analysis of planar grating diffraction," *J. Opt. Soc. Amer.*, vol. 71, no. 7, pp. 811–818, Jul. 1981.

[32] K. Hjort, "Sacrificial etching of III–V compounds for micromechanical devices," *J. Micromech. Microeng.*, vol. 6, no. 4, pp. 370–375, Dec. 1996.

[33] A. Liu, W. Hofmann, and D. Bimberg, "2D analysis of finite size high-contrast gratings for applications in VCSELs," *Opt. Exp.*, vol. 22, no. 10, pp. 11804–11811, May 2014.